JSEE Vol. 26, No. 4, 2024 DOI: 10.48303/jsee.2024.2033543.1106

Research Paper

Seismic Active Earth Pressure during Kahramanmara? Earthquake Using a Time Domain Pseudo-Dynamic Method

***Morteza Jiryaei Sharahi*[1*] *and Mohammad Mobini*[2]**

1. Assistant Professor, Civil Engineering Department, Qom University of Technology, Qom, Iran,
*Corresponding Author; email: jiryaei@yahoo.com
2. M.Sc. Student, Civil Engineering Department, Qom University of Technology, Qom, Iran

Received: 07/07/2024
Accepted: 14/07/2024

Keywords:
Kahramanmara? Earthquake; Seismic Active Pressure; Wall, Seismic Acceleration

ABSTRACT

This study investigates the seismic active pressure induced by the Kahramanmara? earthquake in Türkiye that occurred on February 6, 2023, with a magnitude of 7.7, using a time-domain pseudo-dynamic approach. This methodology enables the incorporation of actual ground motion data from the earthquake into the analysis. Morever, it employs a momentum theory-based technique to precisely identify the critical failure surface. Seismic accelerations recorded at four specific stations located 14, 123, 142 and 237 km away from the earthquake's epicenter, experiencing peak ground accelerations of 0.57g, 0.15g, 1.34g and 0.17g respectively, are utilized to evaluate the seismic active pressure acting on a retaining wall. The results indicate that the proposed approach yields more realistic outcomes compared to conventional methods, particularly in scenarios of significant earthquakes. Besides the peak ground acceleration of the earthquake, which influences the active seismic pressure, the frequency content of the earthquake, and the site's position relative to the fault movement also play crucial roles.

How to cite the article:
Jiryaei Sharahi, M. and Mobini, M. (2024). Seismic Active Earth Pressure during Kahramanmara? Earthquake Using a Time Domain Pseudo-Dynamic Method. *Journal of Seismology and Earthquake Engineering*,*26* (4), 25-35. doi: 10.48303/jsee.2024.2033543.1106

1. Introduction

The determination of the seismic response of geotechnical structures is crucial for ensuring safe design in areas prone to earthquakes. The dynamic behavior of these structures is complex, and utilizing various methods is essential for obtaining a comprehensive understanding of their behavior. While numerical methods offer a detailed description of the dynamic behavior of geotechnical structures, their time-consuming nature and challenges in interpreting results have limited their widespread use within the technical community. On the other hand, the pseudo-static method provides a simplified approximation of the dynamic behavior, neglecting certain factors such as the frequency content of ground motion. Consequently, there is a need for an improved method that considers the impact of ground motion during earthquakes.

This study aims to assess the seismic active earth pressure on rigid retaining walls during Kahramanmara? earthquake, Türkiye on February 6, 2023, with $M_W = 7.7$, by using a time-domain pseudo-dynamic method proposed by Sharahi (2022). Previous research has utilized the pseudo-static method to compute seismic active earth pressure. Mononobe-Okabe developed the pseudo-static method to extend Coulomb's theory for seismic active earth pressure on the rigid retaining wall. Many researchers employed the pseudo-static method to compute seismic active earth pressure behind the retaining wall. But this method does not account for the time-dependent effect and oscillatory nature of earthquakes. To address this limitation, Steedman et al. (1990) introduced a pseudo-dynamic method for the seismic analysis of active thrust on retaining walls. Choudhury and Nimbalkar (2006) introduced the pseudo-dynamic method for calculating the seismic active earth pressure distribution on a rigid retaining wall. This technique was later employed by Ghosh (2010) to determine the seismic active thrust on a battered retaining wall. Bellezza et al. (2012) adapted the pseudo-dynamic method for analyzing submerged backfill, considering both horizontal and vertical acceleration effects as well as amplification. The pseudo-dynamic method has been used by researchers for various earthquake geotechnical issues (Choudhury and Nimbalkar, 2005, 2008; Ghosh, 2007; Ramazan Borujerdi, 2021). Ahmad et al. (2011) Ahmad and Choudhury (2010) investigated the rotational stability of a waterfront retaining wall using the pseudo-dynamic approach, examining the rotational displacement caused by a combination of hydrodynamic pressure and seismic forces. However, a limitation of the pseudo-dynamic method is its inability to satisfy boundary conditions, particularly the assumption of zero shear stress at the soil surface. Additionally, this method assumes a constant acceleration amplification factor throughout the depth of the backfill soil (Ahmadi et al., 2021).

An important development in this field was the introduction of a modified pseudo-dynamic method that addressed the boundary conditions and provided a more accurate representation of the seismic behavior of geotechnical structures (Bellezza, 2014, 2015). Yang and Li (2018) conducted upper bound analysis of 3D static and seismic active earth pressure, contributing to the understanding of the maximum potential earth pressure that retaining walls may experience during seismic events. Sun and Song (2016) performed an active earth pressure analysis based on the normal stress distribution function along the failure surface in soil obeying nonlinear failure criterion. Their study contributes to a better understanding of the soil failure behavior under seismic conditions and its impact on earth pressure. Santhoshkumar and Ghosh (2021) presented a closed-form solution for seismic earth pressure on a bilinear retaining wall using the method of characteristics. Their study offers a practical approach for estimating seismic earth pressure, providing a valuable tool for engineers in seismic design. Halder and Chakraborty (2023) estimated the seismic active earth pressure on the reinforced retaining wall by combining the lower bound finite element limit analysis and the modified pseudo-dynamic method. It is important to note that the modified pseudo-dynamic method has limitations in accurately determining the critical failure surface under seismic conditions. Also, in the modified pseudo-dynamic method, the dynamic response is computed solely for harmonic excitation, thus focusing only on the system's behavior without considering the specific characteristics of the earthquake ground motion. However, the ground motion data recorded during earthquakes are

readily available from databases.

The time-domain pseudo-dynamic method presented by Sharahi (2022) and Sharahi and Mobini (2024) can directly incorporate the earthquake ground acceleration recorded during seismic events as input for calculations. Determining the critical failure surface is based on the momentum of the failure wedge, incorporating strain localization in the backfill soil and also the post-peak reduction in the shear resistance from peak to residual values (Koseki et al., 1998).

In this study, seismic active pressure on the wall due to Kahramanmara? earthquake is assessed using data recorded at stations 4615, 3133, 3135 and 2308 located at 14, 123, 142 and 237 km from epicenter with peak ground acceleration of 0.57g, 0.15g, 1.34g, and 0.17g, and, respectively. Results show that the proposed method provides realistic responses, whereas existing methods provide unrealistic responses in the case of a large earthquake. Moreover, in addition to the peak ground acceleration of the earthquake, which affects the active seismic pressure, the frequency content of the earthquake acceleration and the site's position relative to the fault movement are also influencing factors.

2. Method of Analysis

The soil's viscoelastic properties are modeled using the Kelvin-Voigt model, which combines a spring and a viscous dashpot in parallel to represent the material's elastic behavior and damping ratio. The stress-strain relationship for a Kelvin-Voigt material can be described as (Sharahi, 2022):

$$\tau = G\gamma' + \eta_s \frac{\partial \gamma}{\partial t} \tag{1}$$

$$\eta_s = \frac{2G\xi}{\omega} \tag{2}$$

where, t denotes time; τ stands for shear stress; γ' represents shear strain; η_s and G indicate viscous damping and soil shear modulus, respectively; while ω and ξ refer to the angular frequency and damping ratio of the S-wave. The equation governing the propagation of stress waves through a viscoelastic medium in vector form can be expressed as (Sharahi, 2022):

$$\rho \frac{\partial^2 \bar{u}}{\partial t^2} = \left\{ (\lambda + G) + (\eta_l + \eta_s) \frac{\partial}{\partial t} \right\} \text{grad}(\kappa) + \left(G + \eta_s \frac{\partial}{\partial t} \right) \nabla^2 \bar{u} \tag{3}$$

where ρ, λ, η_l represent the density, the first Lame constant, and the viscosity component. $\bar{u}$ stands for the displacement vector and $\kappa = \text{div}(\bar{u})$. For the vertical propagation of a plane wave in a Kelvin-Voigt homogeneous medium, Equation (3) can be simplified as (Bellezza, 2015):

$$\rho \frac{\partial^2 u_h}{\partial^2 t} = G \frac{\partial^2 u_h}{\partial^2 z} + \eta_s \frac{\partial^3 u_h}{\partial^2 z \partial t} \tag{4}$$

$$\rho \frac{\partial^2 u_v}{\partial^2 t} = (\lambda + 2G) \frac{\partial^2 u_v}{\partial^2 z} + (\eta_l + 2\eta_s) \frac{\partial^3 u_v}{\partial^2 z \partial t} \tag{5}$$

where u_h and u_v denote horizontal and vertical components of the displacement.

Sharahi (2022) obtained the below solution for Equation (4) by assuming $u_{hb} = u_{h0} e^{i\omega t}$ as the harmonic base displacement:

$$a_h(z,t) = \frac{\partial^2 u}{\partial t^2} = a_{h0} e^{i\omega t} \frac{\cos k_s^* z}{\cos k_s^* h} \tag{6}$$

where h and z represent the thickness of the soil layer and the depth from the ground surface as shown in Figure (1). u_{h0} stands for the horizontal displacement amplitude at the rigid base, and k_s^* is the complex wavenumber:

$$k_s^* = \frac{\omega}{\sqrt{\frac{G^*}{\rho}}} = \frac{\omega}{V_s^*} \tag{7}$$

G^* and V_s^* represent the complex shear modulus

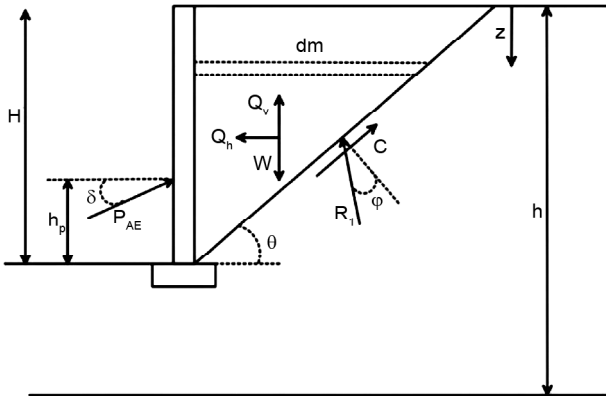

Figure 1. System of forces acting on the soil wedge.

and the shear wave velocity:

$$G^* = G(1+2\xi i) \tag{8}$$

$$V_s^* = \sqrt{\frac{G}{\rho}}\left(\sqrt{1+2\xi i}\right) \tag{9}$$

a_{h0} represents the horizontal harmonic acceleration at the rigid base ($a_{h0} = -u_{h0}\omega^2$). a_h denotes the horizontal acceleration at a depth of z. Similarly, Equation (5) is solved for a harmonic vertical vibration assuming $u_{vb} = a_{v0}\, e^{i\omega t}$ as the base motion:

$$a_v(z,t) = a_{v0}\, e^{i\omega t}\frac{cosk_p^* z}{cosk_p^* h} \tag{10}$$

where k_p^* represents the complex wavenumber corresponding to P-wave with propagation velocity of V_p^*:

$$k_p^* = \frac{\omega}{V_p^*} \tag{11}$$

a_{v0} denotes the vertical harmonic base acceleration. a_v is the acceleration at a depth of z.

Transfer functions (or amplification factors) f_{ha} and f_{va} corresponding to horizontal and vertical accelerations can be obtained as (Sharahi, 2022):

$$f_{ha}(z,\omega) = \frac{a_h}{a_{h0}e^{i\omega t}} = \frac{cosk_s^* z}{cosk_s^* h} \tag{12}$$

$$f_{va}(z,\beta) = \frac{a_v}{a_{v0}e^{i\omega t}} = \frac{cosk_p^* z}{cosk_p^* h} \tag{13}$$

Transfer functions in Equations (12) and (13) depend on z, k_s^*, k_p^*, and h. These transfer functions can be applied to obtain the motion at the ground surface or at a depth of z from the input excitation.

The modified pseudo-dynamic method incorporates wave propagation, allowing for the extension of the transfer function concept to derive inertial forces or weighted average accelerations. Weighted average accelerations are calculated by dividing the inertial force acting on the failure wedge by the mass of the failure wedge. In Figure (1), the failure is depicted as a plane inclined at an angle of θ to the horizontal plane. The incremental mass, dm, of a thin element at a depth z from the surface is determined as:

$$dm(z) = \frac{\gamma}{g}.\frac{H-z}{\tan\theta}dz \tag{14}$$

where g represents acceleration due to gravity; H denotes the wall height.

The total horizontal inertial forces, denoted as Q_h, acting on the failure wedge can be obtained as:

$$Q_h(w) = \int a_h(z,t)dm = \frac{\rho a_{h0}e^{i\omega t}}{\tan\theta\cos(k_s^* h)}$$
$$\int_{z=0}^{z=H}(H-z)*\cos(k_s^* z)dz = \frac{\rho a_{h0}e^{i\omega t}}{\tan\theta\cos(k_s^* h)}\times \tag{15}$$
$$\left[\frac{H}{k_s^*}\sin(k_s^* z) - \frac{z}{k_s^*}\sin(k_s^* z) - \frac{1}{k_s^{*2}}\cos(k_s^* z)\right]_0^H =$$
$$\frac{\rho a_{h0}e^{i\omega t}\left(1-\cos(k_s^* H)\right)}{\tan\theta\cos(k_s^* h)(k_s^*)^2}$$

by assuming:

$$Q_h(w) = a_{h,av}\frac{W}{g} \tag{16}$$

$$W = \frac{1}{2}\gamma H^2\cot\theta \tag{17}$$

Therefore,

$$a_{h,av} = \frac{2\,a_{h0}e^{i\omega t}\left(1-\cos(k_s^* H)\right)}{\cos(k_s^* h)(k_s^* H)^2} \tag{18}$$

$$f_h = \frac{a_{h,av}}{a_{h0}e^{i\omega t}} = \frac{2\left(1-\cos(k_s^* H)\right)}{\cos(k_s^* h)(k_s^* H)^2} \tag{19}$$

where f_h is the transfer function corresponding to the horizontal inertia force, ah,av represents weighted average horizontal acceleration. W represents the weight of the failure wedge.

The transfer function in Equation (19) is established based on a system subjected to harmonic excitation at an angular frequency of ω. This transfer function is used for determining inertial forces resulting from earthquake ground motion via the Fourier series. Consequently, to compute inertial forces, each frequency component of the seismic acceleration in the Fourier domain is multiplied by the corresponding transfer function value. By applying the inverse Fourier transform:

$$a_{heav}(t) = IFT(f_h A_h) \tag{20}$$

$$Q_{he}(t) = a_{heav}(t)\frac{W}{g} \tag{21}$$

where *IFT* stands for Inverse Fourier Transform, Q_{he} is the total horizontal inertial force due to the seismic excitation, A_h represent the transformed horizontal component of the earthquake acceleration. a_{heav}(t) represent the time-domain horizontal component of the weighted average acceleration corresponding to the horizontal inertial force.

Based on Equation (21), it is clear that the inertial force relies on both the weighted average acceleration and the mass of the wedge.

Additionally, according to Equation (20), the weighted average acceleration is influenced by both the earthquake acceleration and the transfer function. It is important to emphasize that the transfer functions represent the system's characteristics.

Similarly, for the vertical direction:

$$Q_{he}(t) = a_{heav}(t)\frac{W}{g}f_v = \frac{2\left(1-\cos(k_p^* H)\right)}{\cos(k_p^* h)(k_p^* H)^2} \tag{22}$$

$$a_{veav}(t) = IFT(f_v A_v) \tag{23}$$

$$Q_{ve}(t) = a_{veav}(t)\frac{W}{g} \tag{24}$$

where f_v is the transfer function corresponding to the vertical inertial force, Q_{ve} represents vertical inertial force due to the seismic excitation, A_v represents the vertical component of the earthquake acceleration in the Fourier domain. $a_{veav}(t)$ denotes the time-domain vertical component of the weighted average acceleration. It is worth noting that f_h (or f_v) is not influenced by the critical failure surface. From Equations (19) and (22), it can be inferred that the behavior of fh is the same as that of f_v.

In Figure (1), the equilibrium of forces acting on the failure wedge results in the following equations

$$\sum F_x^{\rightarrow^+} = 0 \rightarrow P_{AE}\cos\delta - Q_{he} - R_1\sin(\theta-\phi) + \frac{cH}{\sin\theta}\cos\theta = 0 \tag{25}$$

$$\sum F_y^{\downarrow_+} = 0 \rightarrow -P_{AE}\sin\delta - Q_{ve} - R_1\cos(\theta-\phi) - \frac{cH}{\sin\theta}\sin\theta + W = 0 \tag{26}$$

From Equations (25) and (26), the total active thrust acting on the wall can be derived as follows:

$$P_{AE}(t) = \frac{1}{\cos(\delta+\phi-\theta)} \begin{bmatrix} (W - Q_{ve}(t) - cH)\sin(\theta-\phi) \\ +(Q_{he}(t) - cH\cot\theta)\cos(\theta-\phi) \end{bmatrix} \tag{27}$$

where W, R, and P_{AE} denote the weight of the failure wedge, resistance force on the failure plane, and active seismic thrust, respectively. δ, ϕ, and c represent the wall friction angle, the soil friction angle, and the cohesion of the backfill soil, respectively. The value of P_{AE} value depends on c and φ as parameters for shear resistance, θ as the angle of the failure surface relative to the horizontal plane, and either aveav or aheav as weighted average accelerations.

Based on the works of Steedman and Zeng (1990), Choudhury and Nimbalkar (2006), Bellezza (2015), and Sharahi (2022), the seismic active earth pressure distribution can be derived by expressing P_{AE} in relation to the variable z instead of H and then finding the derivative of P_{AE} with respect to z.

$$p_{ae} = \frac{\partial P_{AE}}{\partial z} = \left(\frac{1}{\cos(\delta+\phi-\theta)}\right)\times \begin{bmatrix} \frac{\partial}{\partial z}(W - Q_{ve} - cz)\sin(\theta-\phi) + \\ \frac{\partial}{\partial z}(Q_{he} - cz\cot\theta)\cos(\theta-\phi) \end{bmatrix} \tag{28}$$

$$\frac{\partial W}{\partial z} = \frac{\gamma z}{\tan\theta} \tag{29}$$

$$\frac{\partial Q_{he}}{\partial z} = \frac{\sin(k_s^* z)}{k_s^* z\cos(k_s^* h)}\frac{A_h(w)}{g}\frac{\gamma z}{\tan\theta} \tag{30}$$

$$\frac{\partial Q_{ve}}{\partial z} = \frac{\sin(k_p^* z)}{(k_p^* z)\cos(k_p^* h)}\frac{A_v(\omega)}{g}\frac{\gamma z}{\tan\theta} \tag{31}$$

By replacing Equations (29) to (31) into

Equation (28) yields

$$p_{ae}(z,\omega) = p_{ae\gamma}(z) + p_{aec}(z) + p_{aeI}(z,\omega) \quad (32)$$

where:

$$p_{ae\gamma}(z) = \left(\frac{1}{\cos(\delta+\phi-\theta)}\right)\frac{\gamma z}{\tan\theta} \quad (33)$$

$$p_{aec}(z) = \left(\frac{-c}{\cos(\delta+\phi-\theta)}\right)\left[\sin(\theta-\phi)+\cos\theta\cos(\theta-\phi)\right] \quad (34)$$

$$p_{aeI}(z,\omega) = \left(\frac{1}{\cos(\delta+\phi-\theta)}\right)\frac{\gamma z}{g\tan\theta}\begin{bmatrix}-f_{vp}A_v(\omega)\sin(\theta-\phi)\\+f_{hp}A_h(w)\cos(\theta-\phi)\end{bmatrix} \quad (36)$$

$$f_{hp} = \frac{\sin(k_s^* z)}{k_s^* z\cos(k_s^* h)} \quad (37)$$

$$f_{vp} = \frac{\sin(k_p^* z)}{(k_p^* z)\cos(k_p^* h)} \quad (38)$$

Horizontal and vertical seismic accelerations in the Fourier domain, denoted as $A_h(\omega)$ and $A_v(\omega)$, are incorporated into Equation (36) to calculate the seismic active pressure distribution along the depth. The components $p_{ae\gamma}$ and p_{aec} in Equation (32) correspond to the weight of the failure wedge and the cohesion of the backfill soil, respectively.

Additionally, p_{aeI} represents the inertial component, incorporating f_{hp} and f_{vp}, as transfer functions associated with the seismic active pressure. By using the inverse Fourier transform:

$$p_{ae}(z,t) = p_{ae\gamma}(z) + p_{aec}(z) + p_{aeI}(z,t) \quad (39)$$

where,

$$p_{aeI}(z,t) = \left(\frac{1}{\cos(\delta+\phi-\theta)}\right)\frac{\gamma z}{g\tan\theta}\times \left[-a_{vp}(t)\sin(\theta-\phi)+a_{hp}(t)\cos(\theta-\phi)\right] \quad (40)$$

Therefore, the total seismic active pressure, p_{ae}, varying with depth and time, can be derived as follows:

$$p_{ae}(z,t) = \left(\frac{1}{\cos(\delta+\phi-\theta)}\right)\frac{\gamma z}{\tan\theta} - \left(\frac{C}{\cos(\delta+\phi-\theta)}\right)\left[\sin(\theta-\phi)+\cot\theta\cos(\theta-\phi)\right] + \left(\frac{1}{\cos(\delta+\phi-\theta)}\right)\frac{\gamma z}{g\tan\theta}\times \left\{IFT\left[-\frac{\sin(k_p^* z)}{(k_p^* z)\cos(k_p^* h)}A_v\right]\sin(\theta-\phi)+ IFT\left[\frac{sin(k_s^* z)}{k_s^* z cos(k_s^* h)}A_h\right]\cos(\theta-\phi)\right\} \quad (41)$$

a_{hp} and a_{vp} represent time-domain weighted acceleration components corresponding to the seismic active pressure. a_{hp} and a_{vp} can be computed by performing the inverse Fourier transform of $f_{hp}\,A_h(\omega)$ and $f_{vp}\,A_v(\omega)$, respectively. The transfer functions associated with pae differ from those of P_{AE} due to pae being dependent on z.

Since soils do not typically resist tensile stresses, seismic active pressure cannot be negative. Tensile cracks may form under tensile stresses, and if cracks connect, there is a risk of failure near the wall. Such failure surfaces have been observed during large earthquakes (Watanabe et al., 2011). Negative seismic active pressures deviate from the actual response; therefore, any negative pressures obtained from Equation (39) should be taken as zero.

Seismic active trust, P_{AE}, can be derived from seismic active pressure using the following equation:

$$P_{AE} = \sum p_{ae}(z,t)\Delta z \quad (42)$$

Seismic active coefficient K_{AE} is obtained as

$$K_{AE} = \frac{2P_{AE}}{\gamma H^2} \quad (43)$$

Equation (42) provides a more precise estimation of the seismic active thrust, P_{AE}, compared to Equation (27) as it eliminates negative seismic active pressures.

Generally, the critical failure surface is the surface that maximizes the seismic active thrust. Several researchers have noted discrepancies between the critical failure surface observed in

experiments and the analytical results (Watanabe et al., 2011). The failure mechanism under dynamic conditions may differ from that under static conditions. The motion of the wedge leading to failure is influenced by both the seismic active thrust and the total mass. The P_{AE}/M ratio is primarily used to determine the critical failure surface, instead of P_{AE} alone. As the θ value decreases, the wedge mass increases considerably, making it difficult for the heavy wedge to move due to its high weight. Conversely, P_{AE} decreases as the θ value increases, preventing failure from occurring.

Strain localization in the backfill soil and the subsequent post-peak reduction in shear resistance from peak to residual values (Koseki et al., 1998) impact the seismic active pressure. The determination of the critical angle of failure involves two steps: before the initial failure formation, when there is no movement of the failure wedge, and after the initial failure formation, which involves the movement of the failure wedge. Prior to failure, maximizing PAE identifies the initial failure surface among various angles, while after the initial failure surface forms, the maximum value of P_{AE}/M indicates the critical failure surface. To establish the critical failure surface, the peak frictional angle ($\varphi = \varphi_p$) is initially chosen to maximize P_{AE} and determine the initial failure angle at each time interval within a range of θ from 1° to 89° with steps of 0.5°. Once the initial failure angle at any given time interval is determined, the residual frictional angle ($\varphi = \varphi_r$) is selected in the subsequent phase. In this phase, the critical failure surface is derived by maximizing P_{AE}/M during the earthquake. In the course of the calculation process, the critical failure surface is assumed to be constant, considering the uniqueness of the failure surface.

As mentioned earlier, in addition to the seismic active thrust, the mass of the wedge also plays a significant role in determining the critical failure surface. Note that the verification of the proposed method by comparison with the experimental and analytical results has been carefully demonstrated in the previous work (Sharahi, 2022). A code for calculating the proposed equations is provided using MATLAB.

3. Results and Discusion

Table (1) shows the peak ground acceleration and distance from the earthquake epicenter of selected stations. It is important to note that the ground acceleration values are influenced by factors other than just the epicentral distance. Station 3133 is closer to the epicenter compared to Station 3135; however, due to being located on the Arabian plate, its PGA is lower. Station 2308 is much farther from the epicenter compared to Station 3133, but it does not have lower acceleration due to being located on the Anatolian sub-plate. Station 3135 is located on the Anatolian plate, and the East Anatolian Fault is oriented towards this station, therefore, it has a much higher pulse compared to Station 4615. Figure (2) also illustrates the location of these chosen stations on the map. The seismic accelerations captured at these stations during the 7.7 magnitude Kahramanmara? earthquake are utilized in this study. The horizontal and vertical seismic accelerations recorded during this earthquake are depicted in Figure (3).

Table 1. Epicentral distance and PGA of selected stations.

Station Code	Epicentral Distance (km)	Horizontal (EW) PGA (g)
4615	14	0.57
3133	123	0.15
3135	142	1.34
2308	237	0.17

The study considers a retaining wall with a height of $H = 4$ m and a backfill soil characterized by a peak friction angle of $\varphi_p = 35°$ and a residual friction angle $\varphi_r = 30°$. In addition to this, a shear wave velocity of $V_s = 250$ m/s, a relationship between P-wave velocity (V_p) and S-wave velocity (V_s) given by $V_p = 1.87\ V_s$, a damping ratio of 10%, and a unit weight of $\gamma = 17$ kN/m^3 are assumed. The friction angle at the wall-soil interface is chosen to be half of the soil's friction angle.

Using the proposed method, values of θ_{cr} and K_{AE} are calculated for the different seismic accelerations. Table (2) shows the values of θ_{cr} and K_{AE} based on the proposed method and based on maximizing P_{ae}.

By maximizing the seismic active thrust, a critical angle of $\theta_{cr} = 1$ degree is obtained for

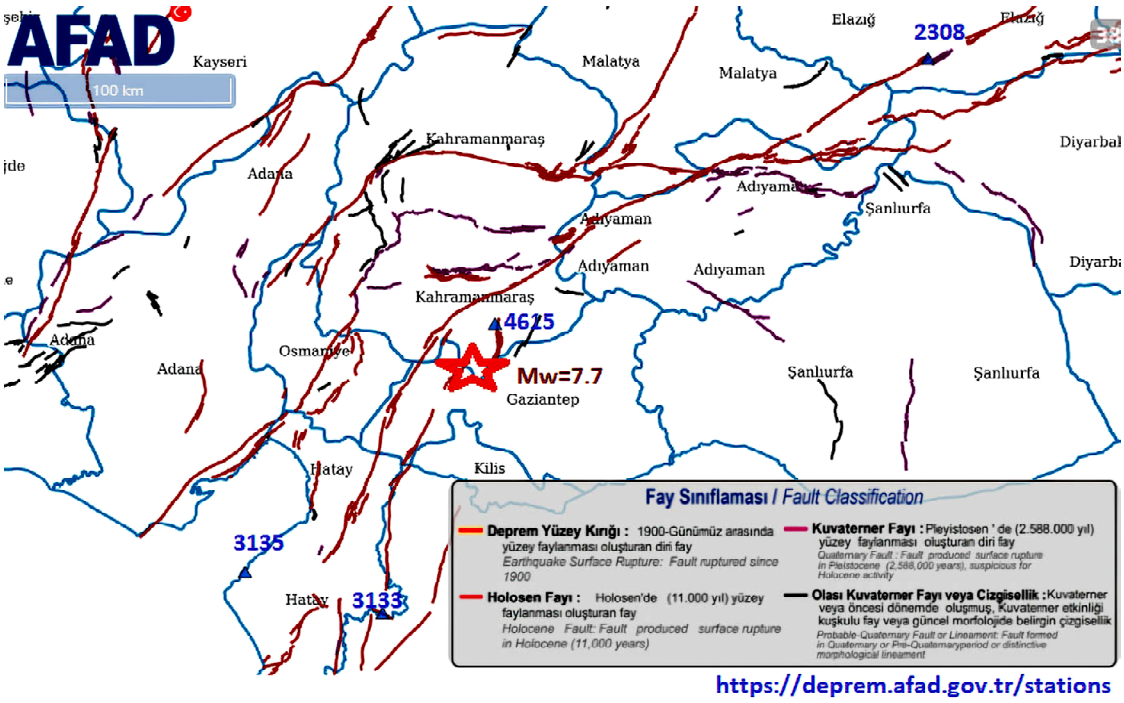

Figure 2. Location of selected stations (AFAD stations).

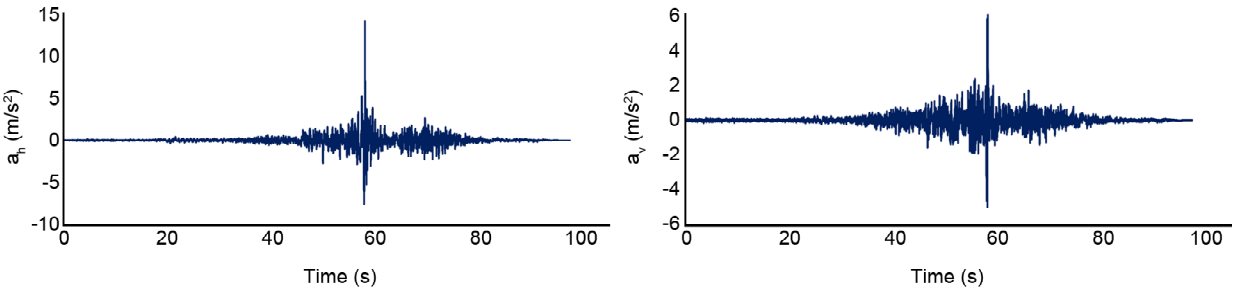

(a) Horizontal Components (b) Vertical Components

Figure 3. Seismic accelerations recorded at station of 3135.

Table 2. alues of θ_{cr} and $K_{AE\text{-}max}$ based on the proposed method and based on maximizing P_{ae}.

Station Name	θ_{cr}		$K_{AE\text{-}max}$	
	Pae-Based	Present Study	Pae-Based	Present Study
3135	1°	69°	30.78	0.61
4615	43°	56°	0.42	0.43
2308	51°	60°	0.35	0.38
3133	55°	56°	0.31	0.36

station 3135, and a seismic active coefficient value of $K_{AE\text{-max}} = 30.78$, which is unrealistic and very high. However, if calculated according to the proposed method, more realistic values (θ_{cr} =69°, $K_{ae\text{-max}} = 0.61$) are obtained because the mass and motion of the failure wedge are also considered in the proposed method. Both methods yield nearly identical results at stations 4615, 3133 and 2308 due to the lower acceleration at these stations.

Consequently, the proposed method offers more accurate solutions for both high and low acceleration conditions. The time history of K_{AE} for station 3135 during the earthquake is shown in Figure (4). A noticeable change in the K_{AE} trend occurs as a result of the development of the failure surface and the reduction in shear strength.

The time histories of the normalized seismic active pressure distribution at varying depths are depicted in Figures (5) and (6) for all chosen stations during the earthquake. To distinguish various time

steps, the normalized seismic active pressure distribution is represented using different colors. The active pressure corresponding to static conditions is shown in yellow. The seismic active pressure distribution at station 4615, which is closer to the epicenter, is non-linear and has a higher value compared to station 3135. It should be noted that the PGA at station 3135 is higher; however, it occurs as a momentary pulse. Therefore, in addition to the PGA of the earthquake, affecting

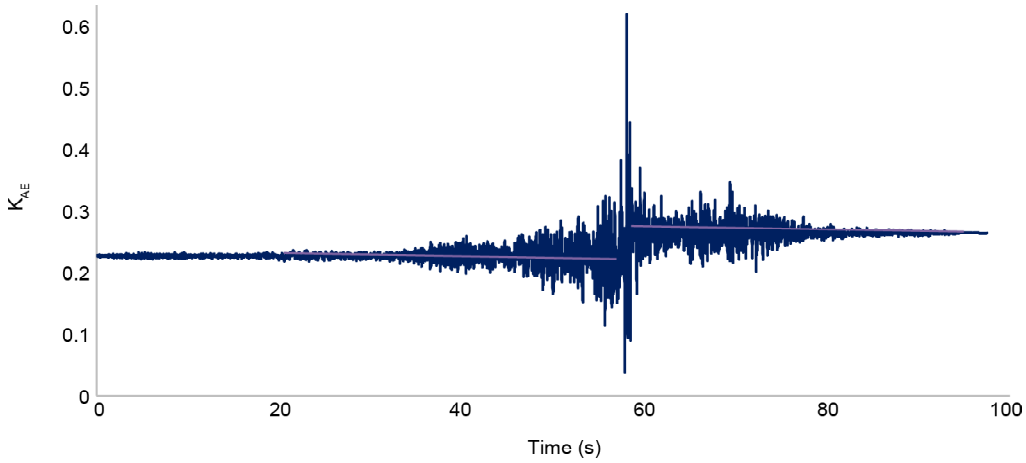

Figure 4. K_{AE} time history during earthquake at station 3135.

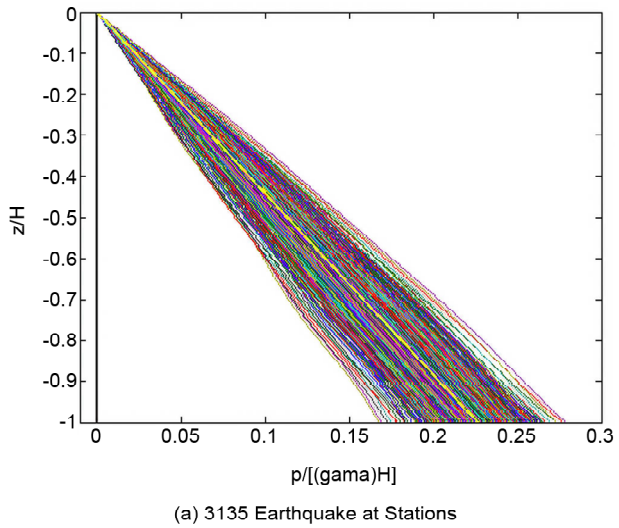

(a) 3135 Earthquake at Stations

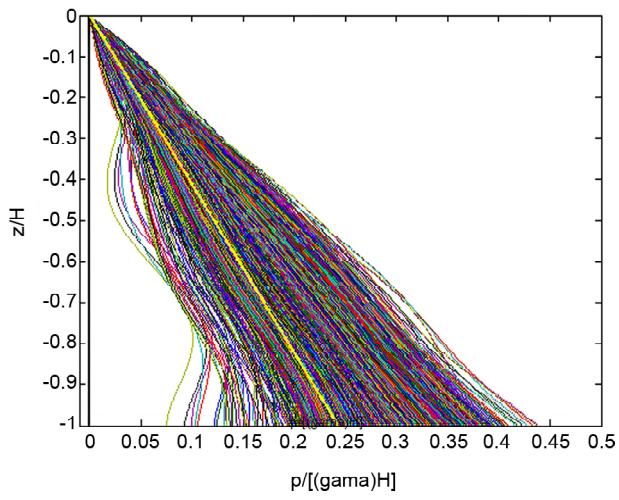

(b) 4615 Earthquake at Stations

Figure 5. Seismic active pressure distribution during the earthquake at stations.

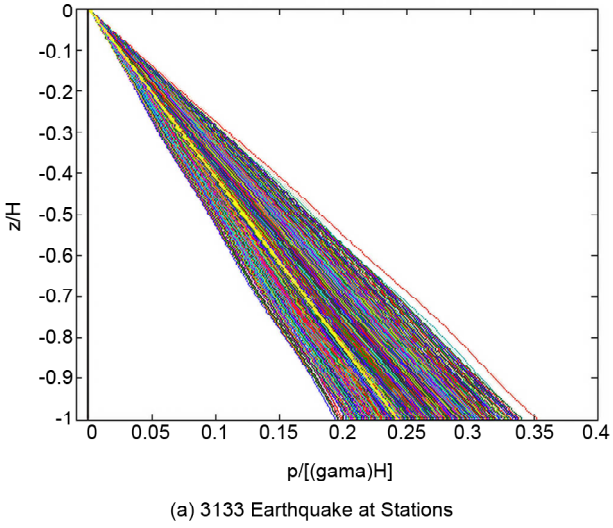

(a) 3133 Earthquake at Stations

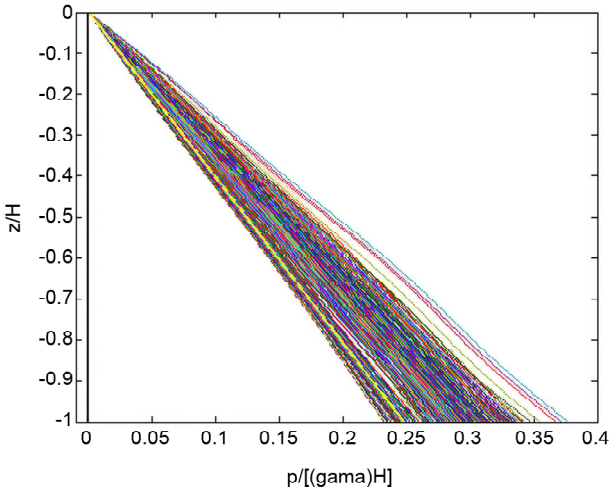

(b) 2308 Earthquake at Stations

Figure 6. Seismic active pressure distribution during the earthquake at stations.

the seismic active pressure, the frequency content of the earthquake acceleration and proximity to the epicenter are also influencing factors.

4. Conclusion

This study assessed the seismic active pressure during the Kahramanmara? earthquake, Türkiye on February 6, 2023, with M_W = 7.7, using a time domain pseudo-dynamic method. This method is capable of incorporating the recorded ground motion during an earthquake into calculations. It also uses a method based on momentum theory to determine the critical failure surface accurately. Seismic accelerations recorded at four stations with distances of 14, 123, 142 and 237 km from the earthquake epicenter were used to analysis seismic active pressure acting on the wall. The results indicated that the proposed method provides realistic responses, whereas existing methods provide unrealistic responses in the case of a large earthquake. Also, in addition to the peak-ground acceleration of the earthquake, which affects the active seismic pressure, the frequency content of the earthquake acceleration and proximity to the epicenter are also influencing factors.

References

Ahmad, S. M., Choudhury, D., Bellezza, I., d'Alberto, D., & Fentini, R. (2011). Discussion: Seismic design factor for sliding of waterfront retaining wall. *Proceedings of the Institution of Civil Engineers - Geotechnical Engineering*, *164*(5), 343-345. doi: 10.1680/geng.10.00034

Ahmad Syed, M., & Choudhury, D. (2010). Seismic rotational stability of waterfront retaining wall using pseudodynamic method. *International Journal of Geomechanics*, *10*(1), 45-52. doi: 10.1061/(ASCE)1532-3641(2010)10:1(45)

Ahmadi, M., Jiryaei Sharahi, M., & Badarloo, B. (2021). Seismic analysis of soil-nailed walls using the modified pseudo-dynamic method. *Bulletin of Earthquake Science and Engineering*, *8*(1), 39-52. doi: 10.48303/bese.2021.243867

Bellezza, I. (2014). A new pseudo-dynamic approach for seismic active soil thrust. *Geotechnical and Geological Engineering*, *32*(2), 561-576. doi: 10.1007/s10706-014-9734-y

Bellezza, I. (2015). Seismic active earth pressure on walls using a new pseudo-dynamic approach. *Geotechnical and Geological Engineering*, *33*(4), 795-812. doi: 10.1007/s10706-015-9860-1

Bellezza, I., D'Alberto, D., & Fentini, R. (2012). Pseudo-dynamic approach for active thrust of submerged soils. *Proceedings of the Institution of Civil Engineers - Geotechnical Engineering*, *165*(5), 321-333. doi: 10.1680/geng.10.00103

Choudhury, D., & Nimbalkar, S. (2005). Seismic passive resistance by pseudo-dynamic method. *Géotechnique*, *55*(9), 699-702. doi: 10.1680/geot.2005.55.9.699

Choudhury, D., & Nimbalkar Sanjay, S. (2008). Seismic rotational displacement of gravity walls by pseudodynamic method. *International Journal of Geomechanics*, *8*(3), 169-175. doi: 10.1061/(ASCE)1532-3641(2008)8:3(169)

Choudhury, D., & Nimbalkar, S. S. (2006). Pseudo-dynamic approach of seismic active earth pressure behind retaining wall. *Geotechnical & Geological Engineering*, *24*(5), 1103-1113. doi: 10.1007/s10706-005-1134-x

Ghosh, P. (2007). Seismic passive earth pressure behind non-vertical retaining wall using pseudo-dynamic analysis. *Geotechnical and Geological Engineering*, *25*(6), 693-703. doi: 10.1007/s10706-007-9141-8

Ghosh, S. (2010). Pseudo-dynamic active force and pressure behind battered retaining wall supporting inclined backfill. *Soil Dynamics and Earthquake Engineering*, *30*(11), 1226-1232. doi: 10.1016/j.soildyn.2010.05.003

Halder, K., & Chakraborty, D. (2023). Estimation of seismic active earth pressure on reinforced retaining wall using lower bound limit analysis and modified pseudo-dynamic method. *Geotextiles and Geomembranes*, *51*(1), 100-116. doi: 10.1016/j.geotexmem.2022.10.001

Koseki, J., Tatsuoka, F., Munaf, Y., Tateyama, M., & Kojima, K. (1998). A modified procedure to evaluate active earth pressure at high seismic loads.

Soils and Foundations, *38*, 209-216. doi: 10.3208/sandf.38.Special_209

Ramazan Borujerdi, A., & Jiryaei Sharahi, M. (2021). Seismic bearing capacity of strip footings adjacent to slopes using pseudo dynamic approach. *Mathematics and Computational Sciences*, *2*(1), 17-41. doi: 10.30511/mcs.2021.137964.1009

Santhoshkumar, G., & Ghosh, P. (2021). Closed-form solution for seismic earth pressure on bilinear retaining wall using method of characteristics. *Journal of Earthquake Engineering*, *25*(6), 1171-1190. doi: 10.1080/13632469.2019.1570880

Sharahi, M.J. (2022). Extended pseudodynamic method to assess seismic active pressure under seismic loading. *International Journal of Geomechanics*, *22*(8), 04022122. doi: 10.1061/(ASCE)GM.1943-5622.0002451

Sharahi, M.J., & Mobini, M. (2024). Seismic active pressure during Kahramanmara? Earthquake in Türkiye using a time domain pseudo-dynamic method. *Paper presented at the 9th International Conf. on Seismology and Earthquake Engineering (SEE9) Tehran*.

Steedman, R.S., & Zeng, X. (1990). The influence of phase on the calculation of pseudo-static earth pressure on a retaining wall. *Géotechnique*, *40*(1), 103-112. doi: 10.1680/geot.1990.40.1.103

Sun, Y.-j., & Song, E.-x. (2016). Active earth pressure analysis based on normal stress distribution function along failure surface in soil obeying nonlinear failure criterion. *Acta Geotechnica*, *11*(2), 255-268. doi: 10.1007/s11440-015-0390-z

Watanabe, K., Koseki, J., & Tateyama, M. (2011). Seismic earth pressure exerted on retaining walls under a large seismic load. *Soils and Foundations*, *51*(3), 379-394. doi: 10.3208/sandf.51.379

Yang, X.-L., & Li, Z.-W. (2018). Upper bound analysis of 3D static and seismic active earth pressure. *Soil Dynamics and Earthquake Engineering*, *108*, 18-28. doi: 10.1016/j.soildyn.2018.02.006